Heliyon 10 (2024) e29145

Contents lists available at ScienceDirect

Heliyon

journal homepage: www.cell.com/heliyon

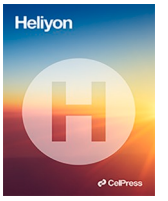

Research article

Study on preparation and properties of silver alloy for Mongolian medicine acupuncture

Bin Xiao [a,c], Jun Wang [b,*], He Yang [c], De-zhi Yang [a], Man Da [a], Ta La [b], Temuqile Temuqile [a,**]

[a] International Mongolian Hospital, Hohhot, Inner Mongolia Autonomous Region, 010021, China
[b] School of Physical Science and Technology, Inner Mongolia University, Hohhot, 010021, China
[c] School of Materials Science and Engineering, Inner Mongolia University of Technology, Hohhot, Inner Mongolia Autonomous Region, 010051, China

ARTICLE INFO

Keywords:
Mongolian medical acupuncture
Silver alloy
Mechanical property
Biocompatibility
Thermoelectric effect

ABSTRACT

The Mongolian medical silver needles often encounter issues of bending, fracturing, and blunting in clinical applications. Similarly, Mongolian warm needles can cause burns on patients due to inaccurate temperature control. In this study, we developed an Ag85Cu15 alloy specifically for acupuncture needles based on material preparation. By incorporating appropriate amounts of Mn and Ti elements, we were able to enhance the mechanical properties and biocompatibility of the acupuncture needles. Compared to commercially available silver needles, this alloy exhibited a significant increase in microhardness up to 210.2 $Hv_{0.2}$ and an improved tensile strength of 880.2 MPa. Furthermore, we designed a thermoelectric effect-based temperature measurement model for precise control of the warm needle's temperature, enhancing the therapeutic effectiveness of the treatment.

1. Introduction

Mongolian medicine is one of the representatives of traditional Mongolian culture [1]. It has summarized a series of fundamental theories and created unique techniques and methods for diagnosis and treatment. Mongolian medical acupuncture therapy, as an important component of traditional Mongolian medicine, uses acupuncture to regulate the body's physiological functions, promote self-repair, and restore health. It has achieved significant therapeutic effects in clinical practice [2].

Mongolian medical acupuncture therapy includes both cold needle and warm needle techniques. Mongolian medical warm acupuncture is a treatment method that combines warm stimulation with acupuncture. It promotes blood circulation and metabolism in the body, accelerates tissue repair and recovery [3,4]. Currently, warm acupuncture has been utilized in clinical practice to treat various conditions including osteoporosis, lumbar disc herniation, knee osteoarthritis, rheumatic cold knee pain, insomnia, ulcerative colitis, and chronic fatigue syndrome [5–11]. During the treatment with silver needles in Mongolian medicine, more attention has been given to the clinical effectiveness of the therapy, while a systematic study on the materials used has been lacking. Silver alloys are widely used in the field of biomedical materials, and numerous studies have reported on their composition, performance optimization methods, and applications [12–16]. Additionally, silver ions or silver nanoparticles were incorporated into biodegradable materials

* Corresponding author.
** Corresponding author.
E-mail addresses: wangjun@imu.edu.cn (J. Wang), tmqyx01@gmail.com (T. Temuqile).

https://doi.org/10.1016/j.heliyon.2024.e29145
Received 28 September 2023; Received in revised form 14 March 2024; Accepted 1 April 2024
Available online 4 April 2024

such as calcium phosphate-based ceramics, polylactic acid (PLA), and polyurethane (PAU) to enhance their mechanical and biological activities [17,18]. Incorporating the essence of systematic research on the aforementioned medical alloy materials into the study of Mongolian medical silver acupuncture needles would be beneficial in aligning Mongolian medical acupuncture therapy with international standards.

Currently, silver needles used in Mongolian medical acupuncture (Mongolian medical silver needle) have unclear composition, poor mechanical properties, and were prone to issues such as oxidation, corrosion, bending, and blunting during use. Traditional resistance wire heating silver needles also have the problem of inaccurate temperature measurement in warm acupuncture therapy. Therefore, the standardization of materials for Mongolian medical silver needles and the development and research of new warm needles were urgent issues to be addressed in both acupuncture theory and clinical applications. Because pure silver is soft and has low strength and hardness, and its color stability is poor, researchers have conducted extensive studies on improving the performance of silver and its alloys. Common methods include alloying, surface treatment, heat treatment, and nano structuring. Adding a small amount of Si in 925 silver promotes alloy deoxidation, increasing the cleanliness and fluidity of the alloy melt, and improving the alloy's resistance to sulfidation corrosion and discoloration [19]. In Ag alloy systems, the introduction of different alloying elements can tune the physical and chemical properties of the alloys, such as stability, electrical thermal transport, and mechanical properties [20–28]. Mn and Ti can enhance the mechanical properties, tarnish resistance, corrosion resistance, and biocompatibility of silver alloys by means of solid solution strengthening, refined crystalline strengthening, corrosion potential, material composition, microstructure alteration, etc. Moreover, both additives were commonly used in other medical alloys due to their non-toxicity [29–32]. However, there has not been a systematic study on the materials of Mongolian medical silver needles. In addition to its good biocompatibility, Cu also boosts the mechanical performance of Ag alloys when added. With this in mind, by studying the amounts of Ti, Mn and Cu added to established medical alloys and their impact on the mechanical properties and biocompatibility of Ag alloys, we can potentially develop superior silver acupuncture needle materials.

As shown in Fig. 1, this paper will optimize the material composition of Mongolian medical silver needle by adding Mn and Ti as additive elements, to explore the effects of component of alloys on the mechanical properties, biocompatibility, and corrosion resistance. By adjusting the additive amount and preparation process, the mechanical properties of the silver alloy used in Mongolian medical acupuncture will be optimized. Additionally, a novel temperature-controlled acupuncture needle model that combines traditional Mongolian medical silver needles with thermoelectric effects has been developed, enabling more precise temperature control and eliminating potential harm to patients caused by inaccurate temperature regulation during moxibustion. Furthermore, the systematic research methods of advanced biomaterials will be introduced into the study of Mongolian medical silver needles. This will contribute to the standardization, intelligentization, and scientific development of Mongolian medical devices, promoting the internationalization of Mongolian medicine.

2. Material and methods

2.1. Sample preparation

Eight samples (It will be referred to as alloy) with different Mn and Ti content were shown in Table 1. The raw materials were

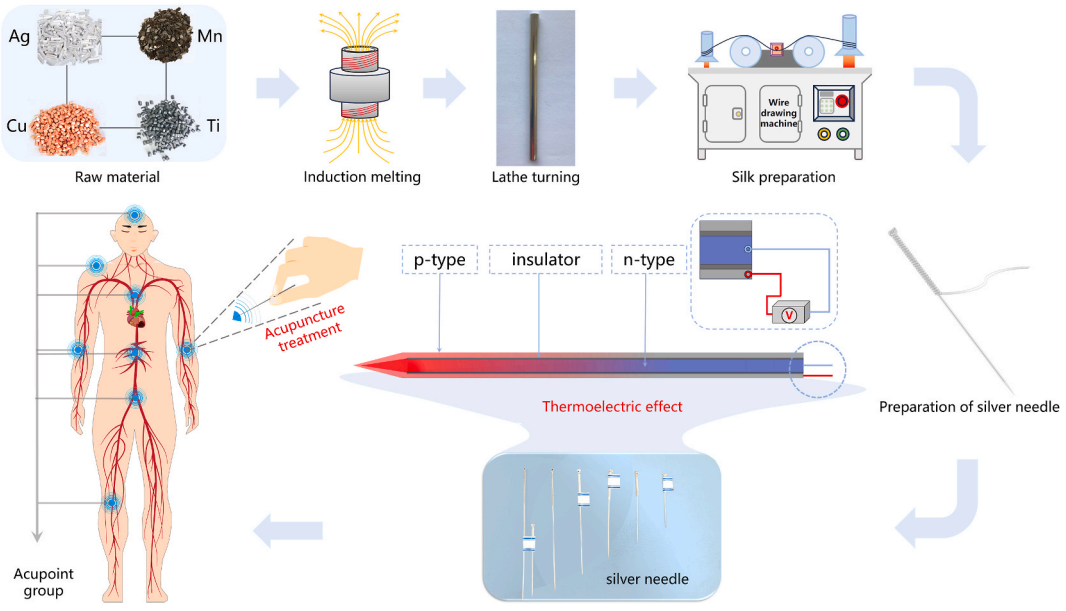

Fig. 1. Schematic of the research methodology and experimental procedure of present work.

weighed according to the specified proportions in Table 1 and then subjected to ultrasonic cleaning and drying. For samples without manganese (Mn) and titanium (Ti), silver (Ag) and copper (Cu) particles were placed into a preheated mold. Vacuum melting was performed at a pressure of 10^{-4} Pa. After 20 min of electromagnetic stirring, the molten solution was cooled to room temperature to obtain the cast alloy. For the samples with added Mn and Ti, the mixture particles of Ag and Cu were placed into a preheated mold and melted through vacuum melting at a pressure of 10^{-2} Pa. Then, different proportions of Mn and Ti particles were added to the molten liquid, followed by 10 min of electromagnetic stirring. After cooling to room temperature, the alloy was obtained as a cast alloy. The cast alloy was remelted and poured into a cylindrical mold with a diameter of 10 mm. After cooling to room temperature, the cast alloy undergone a 4 h homogenization annealing process. The surface scale was removed by machining. A portion of the cylindrical alloy with a thickness of 10 mm was cut using a diamond wire saw for subsequent testing. The remaining portion was subjected to rolling and drawing processes until a wire with a diameter of 3 mm was obtained. The wire was then subjected to multiple cold drawing passes at a speed of 20 m/min, resulting in a wire with a diameter of 1 mm.

2.2. Sample characterization

The D/max 2500pcx X-ray diffractometer (XRD) from RIGAKU Corporation, Japan, was used for phases analysis of the samples in the 2theta range of 20–90°. The metallurgical microscope Axio Observer from ZEISS, Germany, field-emission scanning electron microscope (SEM) LE desktop from Phenom-World, Netherlands, packaged with the energy-dispersive X-ray spectrometer (EDS) Amptek Fast SDD X123, were used for microstructure and composition analysis. The Optima 7000DV Inductively Coupled Plasma (ICP) Mass Spectrometer from PerkinElmer was employed for actual chemical composition analysis of the alloy and detection of ion concentration in immersion experiments. The CMT 2503 microcomputer-controlled electronic universal testing machine from Shenzhen XinSansi Material Testing Co., Ltd was used to test the tensile strength and fracture elongation of the samples. The microhardness testing was carried out using the HXD–1000TM/LCD Vickers hardness tester from Shanghai Taiming Optical Instrument Co., Ltd. Electrochemical testing of the samples in simulated body fluid at 37 °C was performed using the Zennium Pro electrochemical workstation from Zahner, at least three times were repeated in each test to guarantee the reproducibility of the results. The PTM–5 portable Seebeck coefficient tester from Wuhan Jiayitong Technology Co., Ltd was utilized for measuring the Seebeck coefficient and electrical conductivity of the alloy samples.

2.3. Cytotoxicity test

2.3.1. Preparation of the extract

The samples that have been soaked in 75% ethanol for 30 min and then dried and subjected to 30 min of disinfection under a UV lamp on the clean bench were transferred into EP tubes containing 1 ml of complete culture medium (mixture solution of D–MEM medium, 10% FBS fetal bovine serum, and 1 mol% dual-antibiotic pen Strep). The tubes were then placed in a humidified atmosphere at 37 °C with 5% CO_2 for 4 h for soaking. After soaking, the mixture was filtered to obtain the extracted solution. The extracted solution from commercially available silver needles was used as the control group, while the complete culture medium alone was used as the blank group. All three groups of the extracted solution were incubated for 4 h at 37 °C in a humidified atmosphere with 5% CO_2 for further use.

2.3.2. Cytotoxicity test

The cytotoxicity of the extracted solution was assessed using the Cell Counting Kit-8 (CCK–8) technique. The experimental protocol involved employing D–MEM culture medium supplemented with 10% fetal bovine serum (FBS) and 1 mol% penicillin-streptomycin dual antibody. Conforming to the guidelines established in ISO 10993 Part 12 [33], the ratio between the sample's surface area and the volume of the extraction solution was set at 3 cm^2/ml. After subjecting the sterilized alloy to aseptic conditions within a centrifuge tube, it was subsequently combined with pre-prepared culture medium. This amalgamation was then incubated in a CO_2 incubator set at a temperature of 37 °C, with 5% CO_2 concentration, for a duration of 4 h before being transferred to a refrigerated environment at 4 °C. The RAW macrophages seeded onto the cell culture plates with density of 10^5 ml^{-1} was incubated period of 24 h within a CO_2 cell culture incubator. Sequentially, the culture medium present on the plates was substituted with the appropriately diluted extracted solutions, as previously described. After an additional 4 h incubation, the cellular morphology and growth were examined, while simultaneously supplementing the samples with 10 μL of the CCK-8 reagent. Subsequently, the samples were

Table 1
Composition of the experimental materials (wt. %).

Sample's name	Mn	Ti	Cu	Ag
1#	0	0	15	REM
21#	0.1	0	15	REM
22#	0.5	0	15	REM
23#	1	0	15	REM
31#	0.5	0.1	15	REM
32#	0.5	0.5	15	REM
33#	0.5	1	15	REM
34#	0.5	2	15	REM

subjected to an additional 4 h incubation period. Finally, utilizing an enzyme immunoassay analyzer, the absorbance at the wavelength of 450 nm was measured. The relative growth rate (RGR%) of the cells was calculated using the subsequent formula:

$$RGR = \frac{OD_t}{OD_n} \times 100\% \quad (1)$$

OD_t : The absorbance of the extractive solution's constituents, OD_n : The absorbance of the negative control group.

2.4. Characterization of the antibacterial properties

The silver needles were treated with ultrasonic waves in both ultrapure water and anhydrous ethanol three times. After being subjected to high-pressure steam sterilization at 120 °C for 30 min, they were immersed in a simulated body fluid (SBF) and incubated in a 37 °C with 5% CO_2 for 12 h to obtain an extract. The Luria-Bertani (LB) medium for Staphylococcus aureus, consisting of 10 g/L pancreatic digest of gelatin, 10 g/L sodium chloride, 20 g/L nutrient agar, and 5 g/L yeast extract, was prepared by dissolving these components in ultrapure water. The pH of the medium was adjusted to 7.4 using a 1 mol/L sodium hydroxide (NaOH) solution, followed by sterilization in a high-pressure steam sterilizer at 120 °C for 20 min. Monoclonal Staphylococcus aureus was inoculated into the LB medium, and after incubation at 37 °C with 5% CO_2 environment for 12 h, the bacterial suspension was adjusted to a concentration of 10^5 cfu/ml using Phosphate Buffer Solution (PBS). Subsequently, 1 μL of a 1 mol% solution of both penicillin and streptomycin, 1 μL of LB medium, and 1 μL of the extract solution for alloy were uniformly applied onto filter paper disks placed on agar plates, representing the control, blank, and experimental groups, respectively. Following incubation at 37 °C with 5% CO_2 environment for 12 h, photographs of the antibacterial zones in each Petri dish were taken, and the diameter of the zones was measured using Nano Measure 1.2 software. By comparing the sizes of the antibacterial zones, the antimicrobial characteristics were analyzed.

3. Results and discussion

3.1. Effects of added Mn and Ti on microstructure and mechanical properties

Fig. 2 shows the X-ray diffraction patterns of silver alloy cast rod and needle samples (Fig. 2a) with different compositions. Fig. 2 (b) shows that all peaks of samples correspond to the Ag phase (PDF#87–0720) and Cu phase (PDF#85–1326), and no peaks corresponding to Mn and Ti phases. The enlarged plot of the strongest peak in the range of 37.5°–39.0° reveals that as the amount of Mn added to the silver alloy increases, the XRD peak gradually shifts to the right. On the other hand, upon adding Ti to the Mn-added Ag–Cu alloy (sample 22#), it is observed that with increasing Ti content, the XRD diffraction peak shifts to the left. The shift in the X-ray peak positions suggests that the smaller atomic radius of Mn (124 p.m.) and the larger atomic radius of Ti (200 p.m.) is respectively dissolved in Ag (144 p.m.) or Cu (128 p.m.), causing lattice distortion in the matrix.

We measured the average actual solid solution content at three different positions of the samples using Inductively Coupled Plasma Mass Spectrometry (ICP–MS) (Table 2). Compared to the nominal compositions designed in Table 1, there were no significant differences in the mass percentages of the actual composition of alloys with different Mn and Ti contents, indicating the successful solid solution of Mn and Ti into the matrix. The differences in solid solution content among the three different positions of the samples were minimal, suggesting a uniform distribution of the composition after annealing treatment.

Fig. 3 illustrates the influence of Mn and Ti content on the as-cast microstructure of silver alloys. As depicted in Fig. 3a–d, with Mn contents below 1 wt%, the grain size of the silver alloy gradually diminishes as the Mn amount increases. However, upon reaching 1 wt % Mn, the grain size of the alloy starts to increase, accompanied by the emergence of larger dendritic structures. The arrangement of the alloy grains becomes more uniform and orderly when 0.1 wt% of Ti is added on top of 0.5 wt% Mn, as shown in Fig. 3e–h. This phenomenon may potentially be attributed to the ability of Ti to facilitate the homogeneous distribution of the α–Ag solid solution.

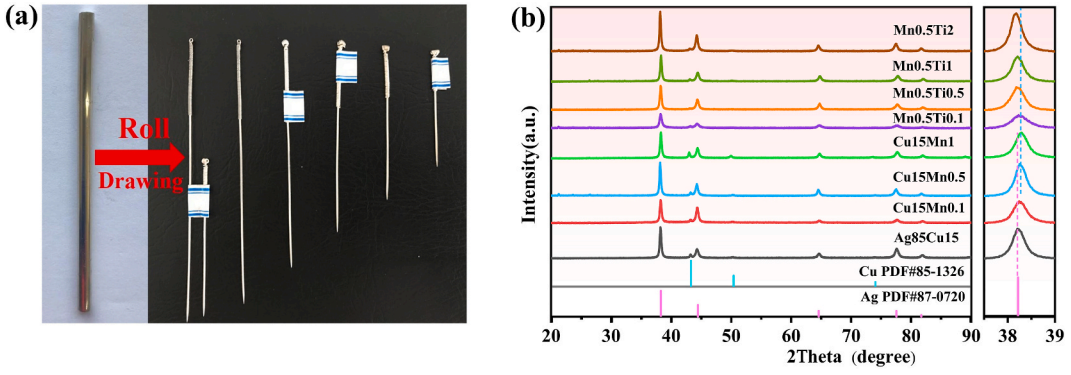

Fig. 2. (a) Photos of cast alloy and silver alloy needles prepared by present work, (b) XRD patterns of cast alloys with different Mn and Ti content.

Table 2
Actual alloy composition measured by ICP-MS (unit: wt.%).

Sample's name	Ag	Cu	Mn	Ti
1#	85.03	14.97	0	0
21#	84.74	15.13	0.13	0
22#	84.65	14.88	0.47	0
23#	83.84	15.07	1.09	0
31#	84.49	14.96	0.47	0.08
32#	84.19	14.83	0.55	0.43
34#	82.34	15.07	0.57	2.02

Fig. 4 presents the SEM images and EDS analysis results. With the increase in Mn and Ti contents, there is a formation of clusters of metallic compounds resulting from the combination of Mn and Cu (Fig. 4d–i), as well as the presence of Ti-rich acicular structures (Fig. 4g–j). The association of Mn and Cu restrains the dislocation movement along the grain boundaries, further enhancing their orderliness [34]. while the presence of Ti assists in suppressing the recrystallization of Ag–Cu alloy grains [35]. The Ti-rich acicular structures are possibly formed through the reaction between Cu, exceeding the solid solubility limit of 14.1 % in Ag, and Ti, resulting in intermetallic TiCu compounds.

The EDS elemental mapping results presented in Fig. 5 reveal that in the SEM images without and with the addition of Ti, the gray regions depict the Ag matrix, while the black regions portray the interconnected network structure forged by the union of Cu and Ag (Fig. 5a and b). Notably, the distribution of Ti elements within the Ti-rich phase appears more pronounced in samples 32# and 34# (Fig. 5c and d).

The cross-sectional SEM images in Fig. 6 depict the alloy wire after the rolling and drawing processes (drawn state). After drawing, the matrix grains elongate while the Cu-rich phase contracts, exhibiting a similar grain size variation trend to that of the as-cast silver alloy (Fig. 6a–d). The matrix grains and acicular structure of the Ti-added samples are elongated into flattened lozenge-shaped structures. This results in localized fracture, grain refinement, and an increase in dislocation density (Fig. 6e–h).

Fig. 7 presents SEM images of the longitudinal cross-section of the 22# sample after drawing. The grains of alloy extend continuously in the drawing direction, forming a wavy slip band (in the yellow dashed boxes in Fig. 7a), indicating multi-system transverse slip. The drawing process leads to a more uniform grain distribution, with the matrix and Cu-rich phase exhibiting a uniform layered distribution (Fig. 7b).

Fig. 8 exhibits cross-sectional SEM images and corresponding EDS mapping images. The Mn and Ti-added samples display smaller grain sizes compared to the alloy without addition. Moreover, as the Ti content increases, the localized aggregation of Ti intensifies, leading to Cu aggregation in the same positions. This finding further confirms the earlier mentioned formation of TiCu alloy compounds.

Fig. 9 illustrates the mechanical properties of cast-alloy and alloy wire with different compositions. Increased Mn content results in higher microhardness in the cast silver alloy (Fig. 9a), which is attributed to grain refinement and Mn–Cu clustering. In addition, the added Mn induces lattice distortion, leading to the formation of numerous dislocation stacks at grain boundaries, which strengthening the grain boundaries and consequently increasing the microhardness of the silver alloy. Hardness also increases with increasing Ti content. The hardness significantly increases when the Ti content exceeds 1 wt% because the TiCu in the grain boundaries of the alloy creates strengthening regions that effectively hinder grain boundary movement. For a Ti content of 2 wt%, the microhardness of the cast-alloy reaches 110.26 $Hv_{0.2}$. After the rolling and drawing processes, all alloys exhibit a significant increase in microhardness (Fig. 9b). This increase can be attributed to grain refinement, lattice distortion, and an increased dislocation density caused by the

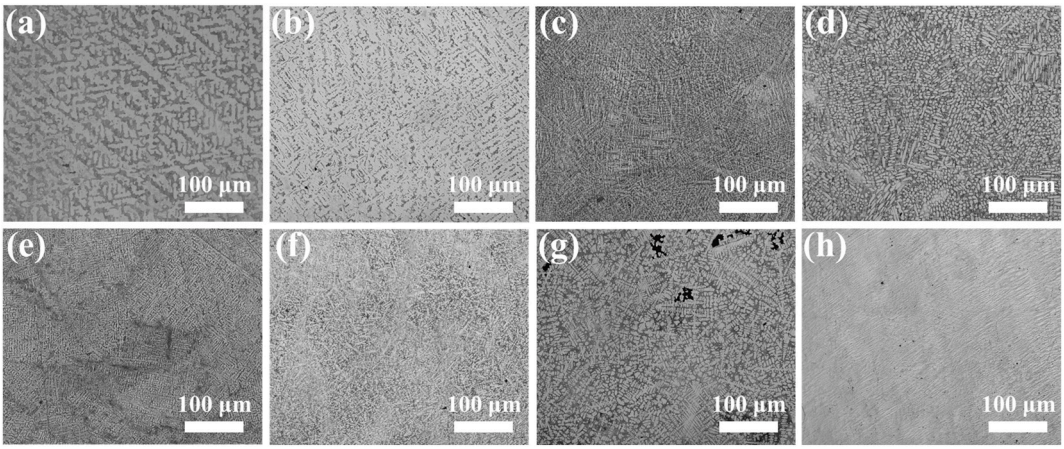

Fig. 3. Microstructure of as-cast silver alloys with different Mn and Ti additions (a) Ag85Cu15, (b) Ag84.9Cu15Mn0.1, (c) Ag84.5Cu15Mn0.5, (d) Ag84Cu15Mn1, (e) Ag84.4Cu15Mn0.5Ti0.1, (f) Ag84Cu15Mn0.5Ti0.5, (g) Ag83.5Cu15Mn0.5Ti1, (h) Ag82.5Cu15Mn0.5Ti2.

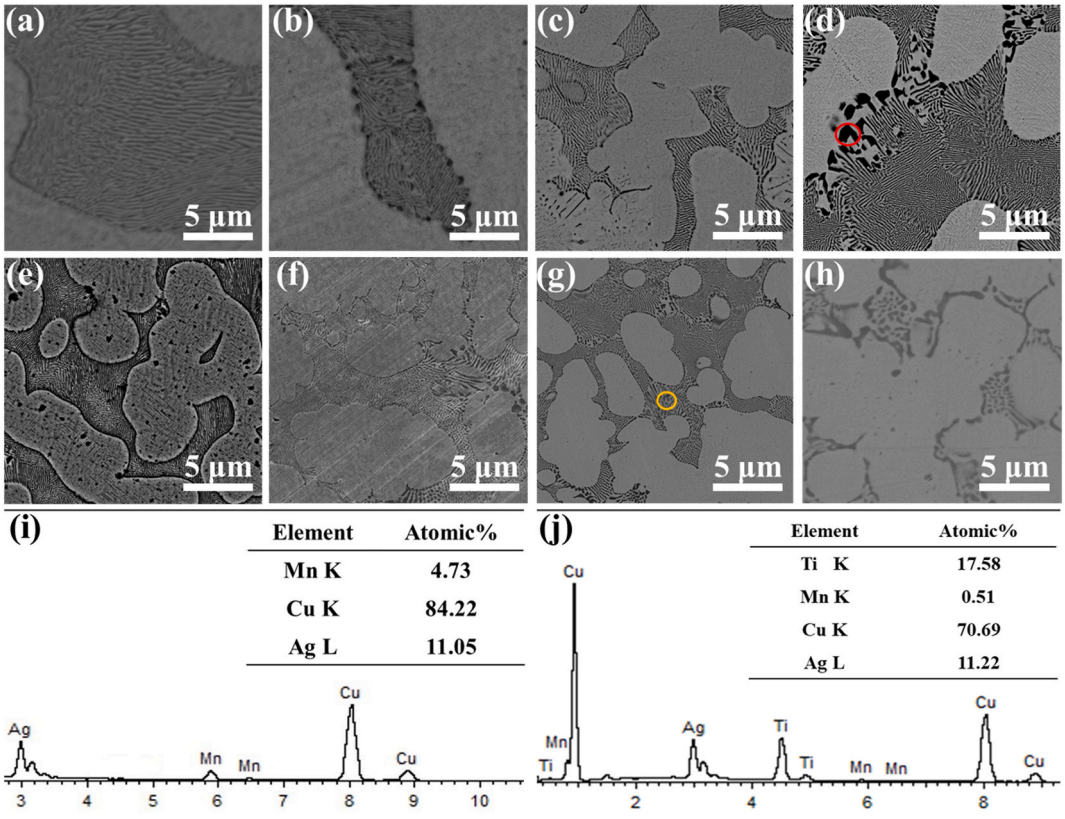

Fig. 4. SEM and EDS point scanning of as-cast silver alloys with different Mn and Ti additions (a) Ag85Cu15, (b) Ag84.9Cu15Mn0.1, (c) Ag84.5Cu15Mn0.5, (d) Ag84Cu15Mn1, (e) Ag84.4Cu15Mn0.5Ti0.1, (f) Ag84Cu15Mn0.5Ti0.5, (g) Ag83.5Cu15Mn0.5Ti1, (h) Ag82.5Cu15Mn0.5Ti2, (i) Ag84Cu15Mn1 EDS point scanning, (j) Ag83.5Cu15Mn0.5Ti1 EDS point scanning.

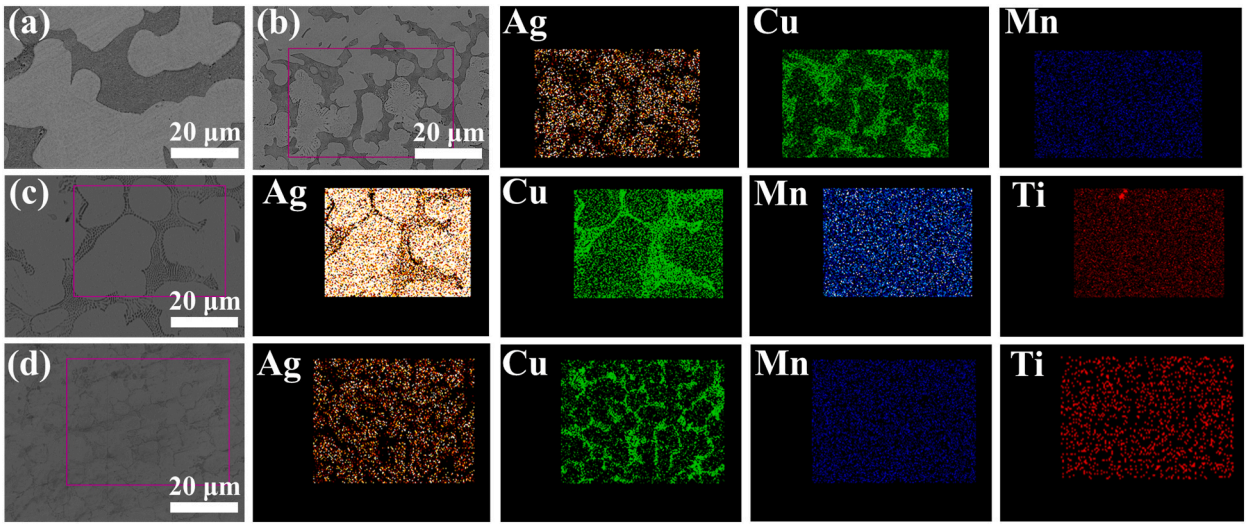

Fig. 5. SEM images and corresponding EDS mapping of as-cast alloy with different Mn and Ti additions (a) Ag85Cu15, (b) Ag84.9Cu15Mn0.5, (c) Ag84.5Cu15Mn0.5Ti1, (d) Ag82.5Cu15Mn0.5Ti2.

mechanical forces during the drawing process. Fig. 9c and d illustrate the tensile strength and fracture elongation of alloys with varying compositions in the drawn state. The tensile strength of our samples surpasses that of commercially available silver acupuncture needles and shows a gradual improvement with increasing Mn content. However, the fracture elongation sharply decreases when the

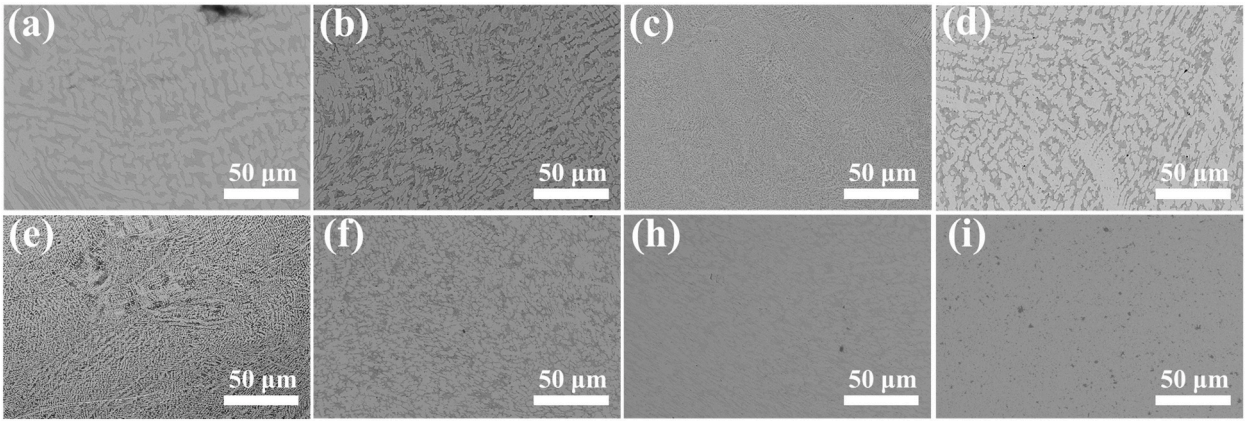

Fig. 6. SEM cross-section of silver alloy with different Mn and Ti (a) Ag85Cu15, (b) Ag84.9Cu15Mn0.1, (c) Ag84.5Cu15Mn0.5, (d) Ag84Cu15Mn1, (e) Ag84.4Cu15Mn0.5Ti0.1, (f)Ag84Cu15Mn0.5Ti0.5, (g) Ag83.5Cu15Mn0.5Ti1, (h)Ag82.5Cu15Mn0.5Ti2.

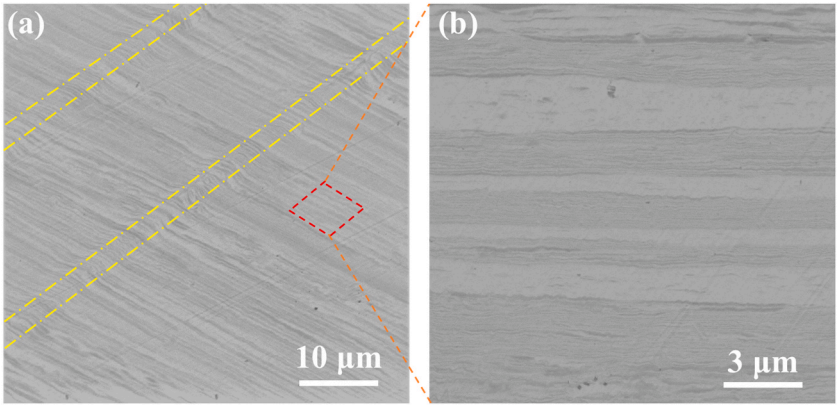

Fig. 7. (a) SEM image of longitudinal section of 22# Ag84.5Cu15Mn0.5 after drawing, (b) enlarged image of position indicated by the red rhomboid in (a).

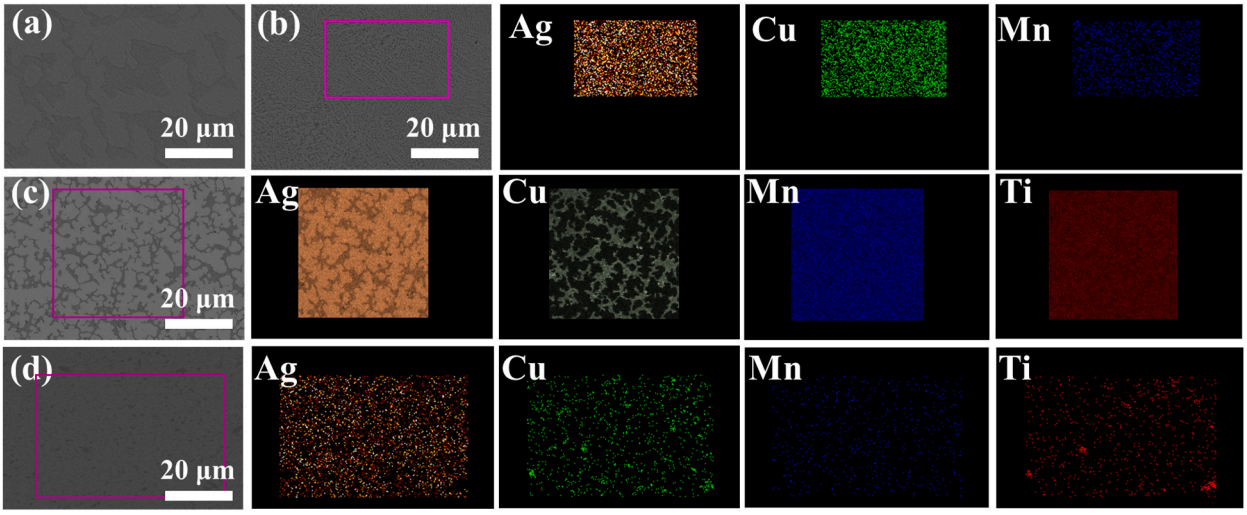

Fig. 8. SEM images and corresponding EDS mapping of alloy wire with different Mn and Ti contents (a) Ag85Cu15, (b) Ag84.5Cu15Mn0.5, (c) Ag83.5Cu15Mn0.5Ti1, (d) Ag82.5Cu15Mn0.5Ti2.

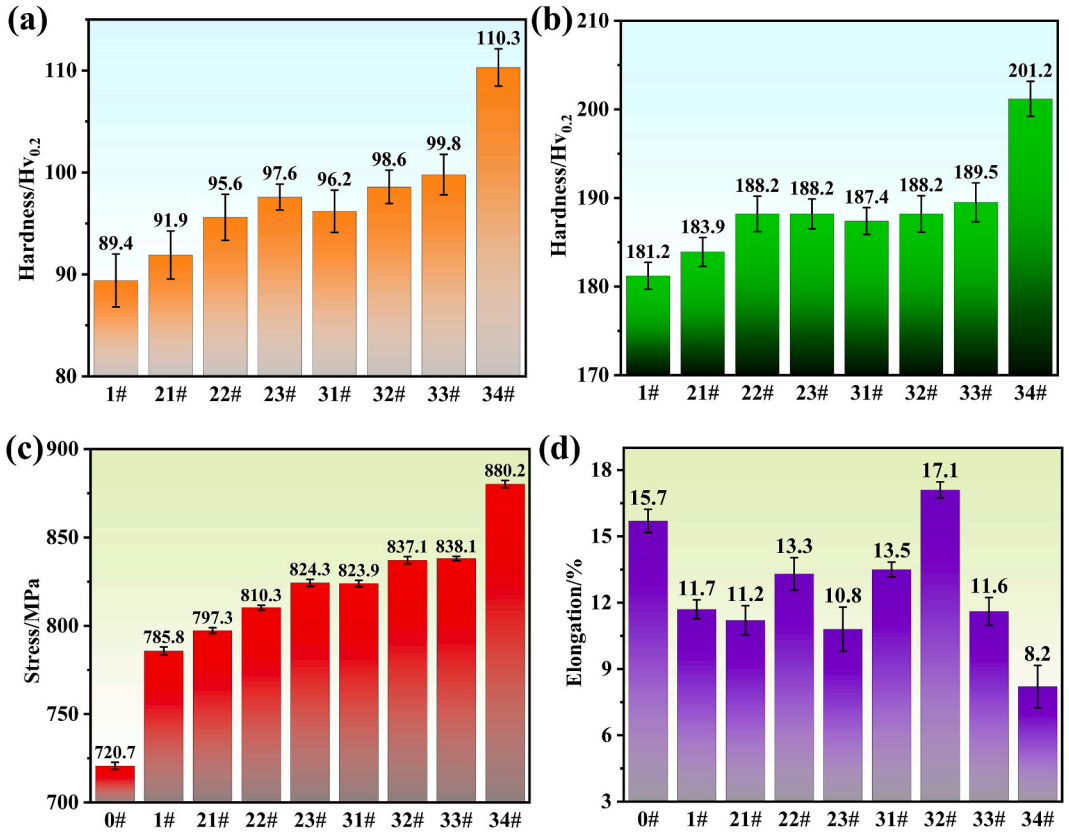

Fig. 9. Mechanical properties of the alloys with different Mn and Ti contents (a) microhardness of as-cast state, (b) microhardness of drawn state, (c) tensile strength, (d) elongation.

Mn content exceeds 0.5 wt%. With an increase in Ti content, the tensile strength gradually improves, while the fracture elongation shows a trend of initially increasing and then decreasing.

The fracture surfaces, as depicted in Fig. 10, exhibit numerous dimples, indicating a characteristic ductile fracture. Notably, Fig. 10b demonstrates that the 22# alloy with a 0.5 wt% Mn addition displays larger "U-shaped" dimples, suggesting enhanced toughness and ductility. Conversely, the 23# alloy with a 1 wt% Mn addition exhibits smaller and smoother dimples, signifying lower material toughness, ductility, and reduced plasticity compared to the 22# alloy. When the Ti content reaches 0.5 wt% (Fig. 10e), the

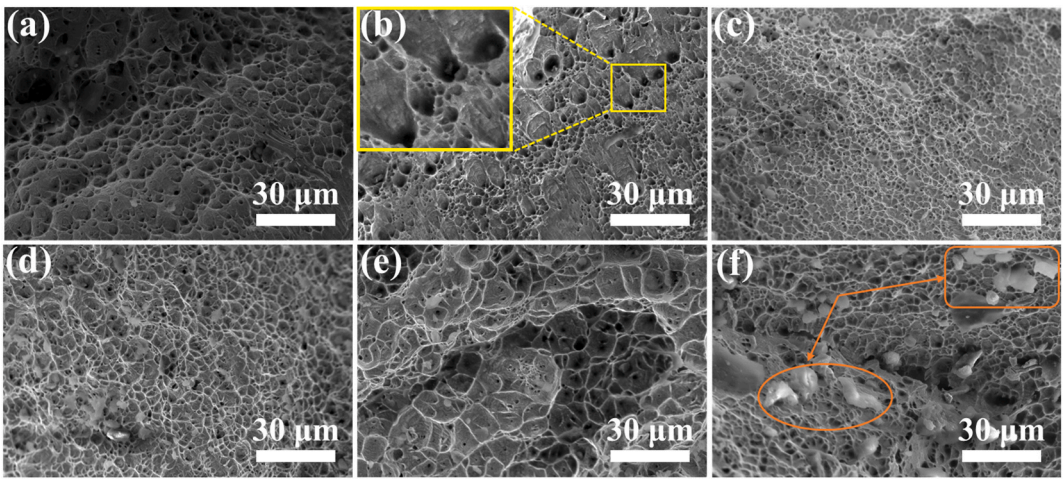

Fig. 10. Morphology of fractured surfaces of drawn alloys with different Mn and Ti contents, (a) Ag85Cu15, (b) Ag84.5Cu15Mn0.5 and corresponding enlarged image (inset), (c) Ag84Cu15Mn1, (d) Ag84.4Cu15Mn0.5Ti0.1, (e) Ag84Cu15Mn0.5Ti0.5, (f) Ag82.5Cu15Mn0.5Ti2.

dimples significantly increase, indicating improved plasticity, in line with the fracture elongation results. However, as the Ti content further increases, granular substances emerge on the fracture surface of the sample (indicated by a dashed frame in Fig. 10f), resulting in a decline in fracture elongation, which is attributed to TiCu compounds [36].

3.2. Corrosion resistance, biocompatibility and thermoelectric properties

Table 3 shows the ion concentrations of Ag, Cu, Mn, and Ti in the solution after immersing alloy wires in simulated body fluid (SBF) at 37 °C for 12 h and 36 h. As the immersion time increases, the rate of ion release exhibits a decreasing trend.

In the immersion solutions of all alloys, the concentration of Cu ions is the highest, while a trace amount of Ag ions is detected. Only a negligible amount of Mn ions is released in the immersion solution of samples containing Mn, and no Ti ions are detected in the immersion solution of the Ti-containing alloy. By comparing the ion release concentrations in alloys with different Mn content, it is observed that the ion release gradually decreased. This may be attributed to the added Mn, which promotes a uniform and fine grain structure in the alloy, forming a dense interface and slowing down the corrosion rate of the alloys. This preliminary observation suggests that the addition of Mn enhances the corrosion resistance of the alloys. Both Mn ions and Ti ions inhibit the dissolution of alloy elements in SBF. This is beneficial for improving the biocompatibility and stability of the silver acupuncture needle. To further elucidate the reasons for the enhanced corrosion resistance and stability of the materials after the addition of Ti and Mn, corrosion tests were conducted in simulated body fluid at 37 °C, as shown in Fig. 11a and Table 4. By fitting the Tafel curve of the dynamic potential polarization, the self-corrosion potential and self-corrosion current were determined, as shown in Table 4. With the addition of Mn and Ti content, the self-corrosion potential of the test samples gradually increased. However, the self-corrosion current showed a trend of initially increasing and then decreasing, with the self-corrosion current of sample 32# (Ag84Cu15Mn0.5Ti0.5) being the lowest. Combined with the trend of self-corrosion potential changes, sample 32# (Ag84Cu15Mn0.5Ti0.5) exhibits the strongest corrosion resistance. The passivation region corresponds to the dashed portion of the Tafel-fitted dynamic potential polarization curve.

The results of the cell toxicity experiment on macrophage cells (RAW) immersed in solutions of different alloys are displayed in Fig. 11b. There is no significant difference in the cell proliferation rate (RGR%) between commercially available silver acupuncture needles and our alloys with varying Mn content. The cell proliferation rates are all above 75%, indicating that the Mn content does not have a significant effect on the cell proliferation rate. However, a statistically significant difference in cell proliferation rates is observed among alloys with different Ti contents. As the Ti content increases, the cell proliferation rate gradually increases, which is associated with a significant decrease in ion release of Ti.

To confirm the non-toxicity of the silver alloy needles prepared in this study, we utilize the Calcein AM/PI double fluorescence staining method to stain cells cultured in the immersion solutions. We then observe the ratio of live and dead cells. Fig. 12 presents the results of cell staining obtained from three identical replicates using commercially available silver acupuncture needles, silver alloy needles prepared in this study, and the complete culture medium. The complete culture medium displays minimal red dead cells but a higher concentration of green live cells compared to other groups. In contrast, the commercially available silver acupuncture needles, as well as the un-added and Mn-added alloys, exhibit a higher number of red dead cells, visually indicated by yellow circles. Increasing the Ti content results in a significant rise in the population of green live cells. In the 34# alloy, the presence of red dead cells is almost negligible, confirming consistency with the CCK–8 experiment results. These findings affirm that the material meets the cytotoxicity requirements for medical metal implants.

Fig. 13 illustrates the antibacterial properties between experimental group containing commercially available silver acupuncture needle and our alloys, compared to the control and blank groups. The size of the antibacterial zones reflects the effectiveness of the antimicrobial activity. The control group exhibits the largest average diameter of 20.68 mm, indicating the strongest antibacterial effect. In contrast, the blank group shows no antibacterial effect. Table 5 illustrates the diameter of the antibacterial zones for the experimental groups. The 0# commercially available silver needle group displays a smaller zone with a diameter of 7.69 mm. As the amount of Mn increases, alloys 1# to 23# exhibit gradually decreasing antibacterial zones. Additionally, as the amount of Ti increases, the alloy loses its antibacterial properties. The immersion test results suggest that the decreasing concentrations of Ag^{+} and Cu^{2+} ions with increasing Mn and Ti content lead to a gradual weakening of the antibacterial effect.

The aforementioned silver needle and constantan wire are combined to form a thermocouple, which exhibits the electrical conductivity and Seebeck coefficient as depicted in Fig. 14a. As the addition amount of Mn and Ti increases, the electrical conductivity gradually declines while the Seebeck coefficient increases. This indicates that added Mn and Ti enhance electron scattering and reduce carrier concentration of alloys. The Seebeck coefficient and electrical conductivity of thermocouple are akin to those of the commercial Cu-constantan thermocouple, demonstrating its suitability for temperature measurement applications. Based on this thermocouple, we design a temperature-sensing silver acupuncture needle that incorporates the thermoelectric effect as illustrated in Fig. 1. Furthermore, we design a high-precision temperature testing equipment for future applications of warming acupuncture, as shown in Fig. 14b. Additional research is necessary to explore the production of temperature-sensing acupuncture silver needles tailored for clinical use. Such studies hold significant research value in the pursuit of the intelligentization of Mongolian medical warm acuputure therapy. Moreover, the influence of Mn and Ti on the silver needle's electrical conductivity and mechanical properties also holds important reference value for the investigation of electrical contact materials and brazing fillers [37–41].

4. Conclusion

In this work, we present a thermometric acupuncture needle model that incorporates the thermoelectric effect into the design of the acupuncture needle. The thermometric acupuncture needle model mainly consisted of Mongolian medical acupuncture needle and

Table 3
Concentration of metal ions in simulated body fluid (SBF) after immersing alloy wires with different composition for 12 h and 36 h.

Sample's name	12 h				36 h			
	Ag mg/L	Cu mg/L	Mn mg/L	Ti mg/L	Ag mg/L	Cu mg/L	Mn mg/L	Ti mg/L
0#	0.008	0.549	0	0	0.013	0.831	0	0
1#	0.026	0.571	0	0	0.032	0.853	0	0
21#	0.031	0.499	0.004	0	0.058	0.835	0.015	0
22#	0.028	0.475	0.001	0	0.031	0.746	0.003	0
23#	0.019	0.401	0.003	0	0.027	0.604	0.023	0
31#	0.012	0.42	0.006	0	0.018	0.635	0.02	0
32#	0.005	0.339	0.003	0	0.011	0.685	0.029	0
33#	0.005	0.367	0.001	0	0.007	0.648	0.02	0
34#	0.001	0.387	0.001	0	0.007	0.611	0.008	0

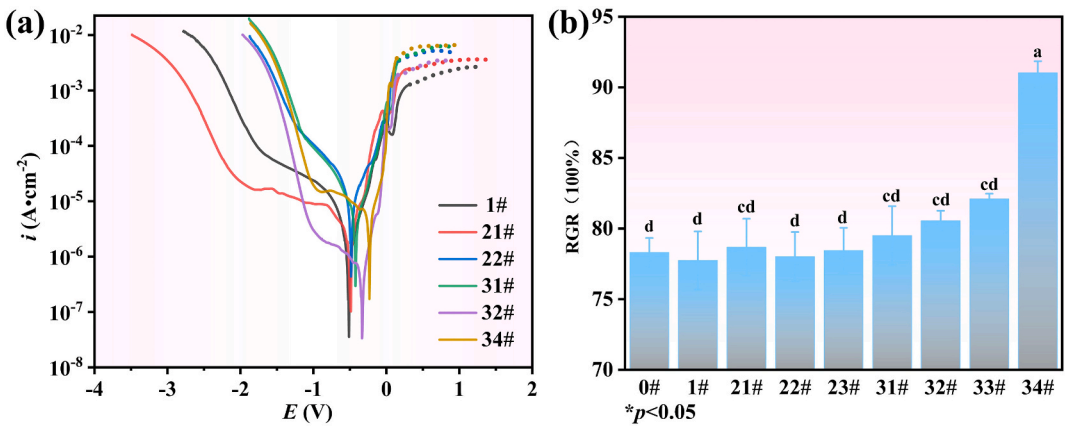

Fig. 11. (a) Tafel plots of different silver as-cast alloys in 37 °C simulated body fluid (SBF), (b) cell proliferation rates of different silver alloy wires.

Table 4
Corrosion potential and corrosion current density of different silver as-cast alloys in 37 °C simulated body fluid (SBF).

Sample's name	*E* (V)	*i* (A•cm^{-2})
1#	−0.522	8.6×10^{-7}
21#	−0.498	1.26×10^{-6}
22#	−0.478	5.34×10^{-6}
31#	−0.42	2.2×10^{-6}
32#	−0.327	2.42×10^{-7}
34#	−0.225	2.69×10^{-6}

constantan wire. The predominant composition of our Mongolian medical acupuncture was Ag85Cu15Mn0.5Ti0.5, synthesized through the vacuum induction melting method. The microhardness and tensile strength of Ag85Cu15Mn0.5Ti0.5 are 188 $Hv_{0.2}$ and 837 MPa, respectively, representing an increase of 11% and 12.1% when compared to Ag85Cu15. The introduction of Mn induces lattice distortion, resulting in the formation of multiple dislocation stacks at grain boundaries. These strengthen the grain boundaries, subsequently enhancing the microhardness of the silver alloy. Mn and Ti both impede the dissolution of alloy elements in SBF, which is advantageous for enhancing the biocompatibility and stability of the silver acupuncture needle. Our designed Ag85Cu15Mn0.5Ti0.5 acupuncture needle exhibits significant mechanical property advantages when compared to commercially available silver acupuncture needles. This study contributes to the standardization and intellectual advancement of acupuncture needles in Mongolian medicine, while also offering practical insights for the functional exploration of acupuncture needles.

CRediT authorship contribution statement

Bin Xiao: Writing – original draft, Writing – review & editing. **Jun Wang:** Writing – review & editing, Writing – original draft, Data curation. **He Yang:** Writing – review & editing. **De-zhi Yang:** Writing – review & editing. **Man Da:** Writing – review & editing. **Ta La:** Writing – review & editing. **Temuqile Temuqile:** Writing – review & editing.

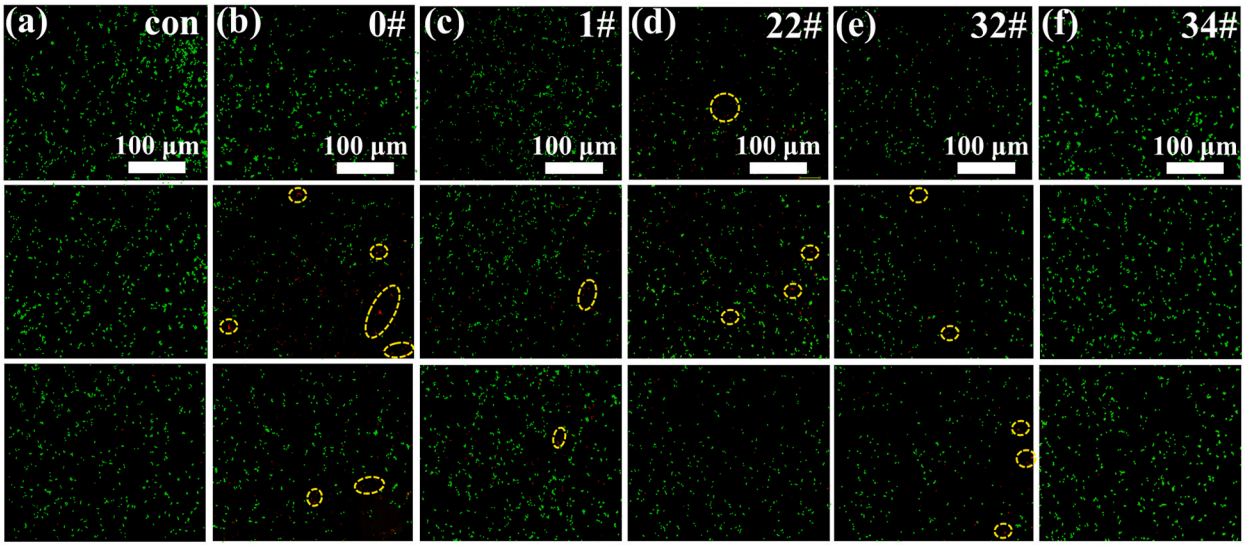

Fig. 12. Staining images of RAW live cells (green) and dead cells (red) for different silver alloy wires (a) complete medium, (b) commercially available silver acupuncture needle, (c) Ag85Cu15, (d) Ag84.5Cu15Mn0.5, (e) Ag83.5Cu15Mn1Ti0.5, (f) Ag82.5Cu15Mn0.5Ti2.

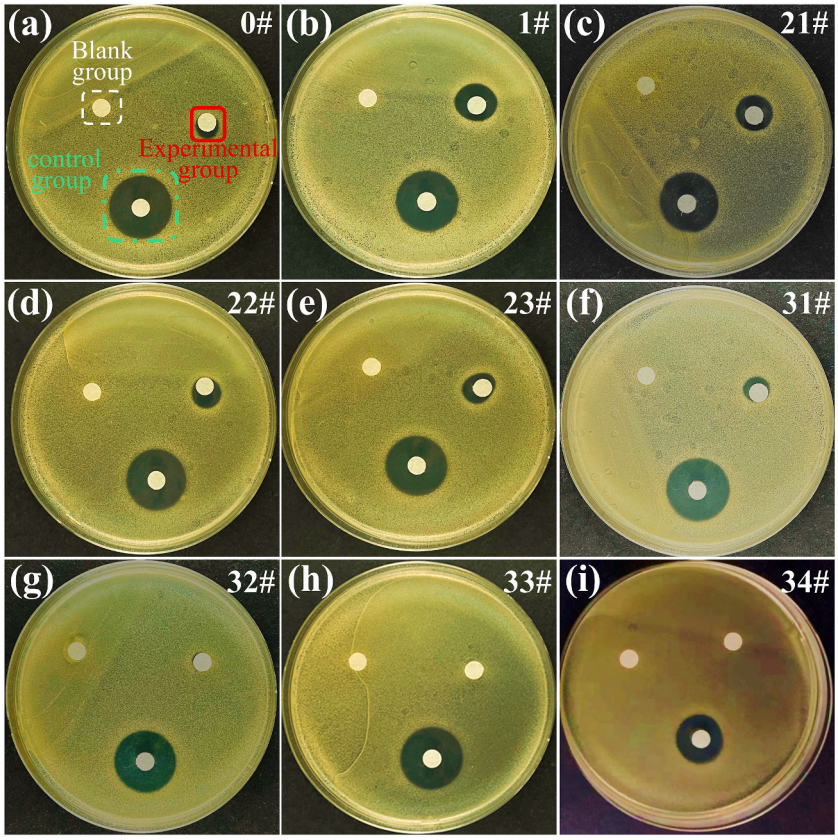

Fig. 13. Antibacterial ring of control and blank groups, along with (a) commercially available silver acupuncture needle, (b) Ag85Cu15, (c) Ag84.9Cu15Mn0.1, (d) Ag84.5Cu15Mn0.5, (e) Ag84Cu15Mn1, (f) Ag84.4Cu15Mn0.5Ti0.1, (g) Ag84Cu15Mn0.5Ti0.5, (h) Ag83.5Cu15Mn0.5Ti1, (i) Ag82.5Cu15Mn0.5Ti2.

Table 5
Diameter of antibacterial ring of commercially available silver acupuncture needle and alloy with different components (mm).

Sample's name	diameter of antibacterial ring (mm)	Sample's name	diameter of antibacterial ring (mm)	Sample's name	diameter of antibacterial ring (mm)
0#	7.69	22#	10.22	32#	0
1#	11.21	23#	10.03	33#	0
21#	10.38	31#	8.43	34#	0

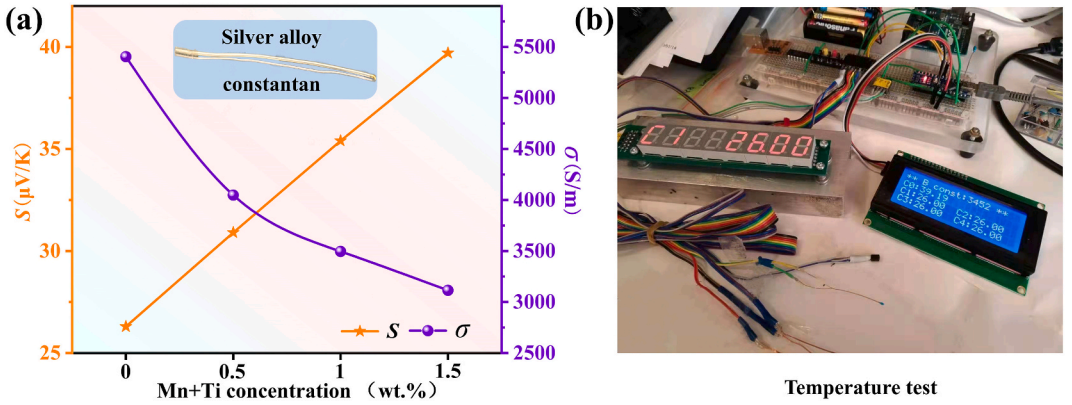

Fig. 14. (a) Seebeck coefficient and electrical conductivity as a function of concentration of added Mn and Ti, along with an image of thermocouple (inset), (b) high precision thermoelectromotive force device.

Declaration of competing interest

The authors declare that they have no known competing financial interests or personal relationships that could have appeared to influence the work reported in this paper.

Acknowledgment

This work was supported by the National Natural Science Foundation of China under No. 52061034; Design of Standardization for High-Performance Mongolian Medicine Silver Needles and High-Precision New Warming Acupuncture Instrument.

References

[1] A. Pitschmann, S. Purevsuren, A. Obmann, D. Natsagdorj, D. Gunbilig, S. Narantuya, C. Kletter, S. Glasl, Traditional Mongolian Medicine: history and status quo, Phytochem. Rev. 12 (2013) 943–959.
[2] G. Shao, W. Xie, X. Jia, R. Bade, Y.B. Xie, R.F. Qi, K.R. Gong, H.H. Bai, L.G. Si, Y.S. Chen, K. Sun, A. Bo, Overview of traditional Mongolian medical warm acupuncture, Aging and Disease 13 (2022) 1030–1041.
[3] A. Bo, L.G. Si, Y.H. Wang, L. Xiu, R.H. Wu, Y.T. Li, R.G.J.Y. Mu, L.T. Ga, M. Miao, F. Shuang, Y.H. Wu, Q. Jin, S.C. Tong, G. Wuyun, W.R.H. Guan, R.G. Mo, S. L. Hu, L.X. Zhang, R. Peng, L.D. Bao, Clinical trial research on Mongolian medical warm acupuncture in treating insomnia, J. Evidence-Based Complementary Altern. Med. 2016 (2016) 6190285.
[4] J.H. Jun, T.-Y. Choi, I. Appleyard, J. Choi, N. Robinson, J.-I. Kim, M.S. Lee, Warm needle acupuncture for osteoarthritis: a systematic review protocol, Eur. J. Integr. Med. 8 (2016) 402–406.
[5] X. Li, Y. Han, J. Cui, P. Yuan, Z. Di, L. Li, Efficacy of warm needle moxibustion on lumbar disc herniation: a meta-analysis, J. Evidence-based complementary, Altern. Med. 21 (2016) 311–319.
[6] A. Bo, L. Si, Y. Wang, L. Bao, H. Yuan, Mechanism of Mongolian medical warm acupuncture in treating insomnia by regulating miR-101a in rats with insomnia, Exp. Ther. Med. 14 (2017) 289–297.
[7] I. Appleyard, N. Crichton, N. Robinson, Warm needle acupuncture vs. needle acupuncture for osteoarthritis of the knee: a pilot study protocol, Eur. J. Integr. Med. 8 (2016) 407–413.
[8] J.H. Jun, T.Y. Choi, N. Robinson, J.Y. Park, E.Y. Jun, K.H. Kim, H.W. Lee, M.S. Lee, S. Park, Warm needle acupuncture for osteoarthritis: a systematic review and meta-analysis, Phytomedicine 106 (2022) 154388.
[9] D. Luo Jr., Y. Liu Jr., Y. Wu Jr., R. Ma Jr., L. Wang Jr., R. Gu Jr., W. Fu, Sr, Warm needle acupuncture in primary osteoporosis management: a systematic review and meta-analysis, Acupunct, Med. 36 (2018) 215–221.
[10] J. Ji, Y. Huang, X.-F. Wang, Z. Ma, H.-G. Wu, H. Im, H.-R. Liu, L.-Y. Wu, J. Li, Review of clinical studies of the treatment of ulcerative colitis using acupuncture and moxibustion, Gastroent. Res. Pract. 2016 (2016) 1–10.
[11] L. Shui, R.N. Yi, Y.J. Wu, S.M. Bai, Q. Si, A.G. Bo, G.R. Wuyun, L.G. Si, Y.S. Chen, J. Lu, Effects of Mongolian warm acupuncture on iNOS/NO and inflammatory cytokines in the Hippocampus of chronic fatigue rats, front. Integr, Neurosci 13 (2019) 78.
[12] F. Paladini, M. Pollini, A. Sannino, L. Ambrosio, Metal-based antibacterial substrates for biomedical applications, Biomacromolecules 16 (2015) 1873–1885.
[13] B. Szaraniec, T. Goryczka, Structure and properties of Ti-Ag alloys produced by powder metallurgy, J. Alloys Compd. 709 (2017) 464–472.
[14] Y. Xie, L. Zhao, Z. Zhang, X. Wang, R. Wang, C. Cui, Fabrication and properties of porous Zn-Ag alloy scaffolds as biodegradable materials, Mater. Chem. Phys. 219 (2018) 433–443.

[15] C. Liu, S. Feng, L. Ma, M. Sun, Z. Wei, J. Wang, Z. Chen, Y. Guo, J. Shi, Q. Wu, An amphiphilic carbonaceous/nanosilver composite-incorporated urinary catheter for long-term combating bacteria and biofilms, ACS Appl. Mater. Interfaces 13 (2021) 38029–38039.
[16] T. Baygar, N. Sarac, A. Ugur, I.R. Karaca, Antimicrobial characteristics and biocompatibility of the surgical sutures coated with biosynthesized silver nanoparticles, Bioorg. Chem. 86 (2019) 254–258.
[17] X.Q. Yu, L.X. Xu, Effects of silver nanoparticles on the in vitro culture and differentiation of human bone marrow-derived mesenchymal cells, Mater. Sci. Forum 852 (2016) 1307–1312.
[18] W. Yin, Z. Zheng, Y.L. Liu, L.N. Wang, C. Shi, L.L. Zhang, S. Liu, W.D. Niu, K. Ting, Z. Bian, Disinfection of infected root canals: nanosilver has good potential, Small Methods 3 (2019) 1900378.
[19] M.J. Yu Q, S.J. Zhong, J.J. Pan, et al., Effect of trace silicon addition on the vulcanization tarnish behavior of 925 silver alloys, Precious Met. 41 (2020) 57–61, issn.1004-0676.2020.03.009.
[20] G. Jin, H. Qin, H. Cao, Y. Qiao, Y. Zhao, X. Peng, X. Zhang, X. Liu, P.K. Chu, Zn/Ag micro-galvanic couples formed on titanium and osseointegration effects in the presence of S. aureus, Biomaterials 65 (2015) 22–31.
[21] Z.B. Li, G.W. Meng, Q. Huang, C.H. Zhu, Z. Zhang, X.D. Li, Galvanic-cell-induced growth of Ag nanosheet-assembled structures as sensitive and reproducible SERS substrates, Chem. Eur J. 18 (2012) 14948–14953.
[22] A.V. Lyasnikova, O.A. Markelova, O.A. Dudareva, V.N. Lyasnikov, A.P. Barabash, S.P. Shpinyak, Comprehensive characterization of plasma-sprayed coatings based silver- and copper-substituted hydroxyapatite, Powder Metall. Met. Ceram. 55 (2016) 328–333.
[23] E. Nisaratanaporn, S. Wongsriruksa, S. Pongsukitwat, G. Lothongkum, Study on the microstructure, mechanical properties, tarnish and corrosion resistance of sterling silver alloyed with manganese, Mat. Sci. Eng. A. 445 (2007) 663–668.
[24] S. Li, B. Gao, S. Yin, G. Tu, G. Zhu, S. Sun, X. Zhu, The effects of RE and Si on the microstructure and corrosion resistance of Zn–6Al–3Mg hot dip coating, Appl. Surf. Sci. 357 (2015) 2004–2012.
[25] Y. WinardiTriyono, N. Muhayat, Effect of post-braze heat treatment on the microstructure and shear strength of cemented carbide and steel using Ag-based alloy, iop conf, Ser.-Mat. Sci 333 (2018) 012039.
[26] M.C. Bernard, E. Dauvergne, M. Evesque, M. Keddam, H. Takenouti, Reduction of silver tarnishing and protection against subsequent corrosion, Corros. Sci. 47 (2005) 663–679.
[27] B. Vaagensmith, Q. Qiao, Effect of synthesis temperature, UV-ozone treatment, and nanowire diameter on the failure of silver nanowire electrodes, IEEE J. Photovolt. 6 (2017) 1549–1553.
[28] S. Yue, X. Ming, B. Jun, Z. Guoquan, G. Weiming, W. Ming, W. Song, Effects of different preparation techniques on mechanical property and electrical conductivity of Cu-8wt% Ag alloy by continuous casting, Rare Met. Mater. Eng. 45 (2016) 1997–2002.
[29] M. Takahashi, M. Kikuchi, Y. Takada, Mechanical properties of dental Ti-Ag alloys with 22.5, 25, 27.5, and 30 mass% Ag, Dent. Mater. J. 34 (2015) 503–507.
[30] M. Alqattan, L. Peters, F. Yang, L. Bolzoni, Microstructure, mechanical behaviour and antibacterial activity of biomedical Ti-xMn-yCu alloys, J. Alloys Compd. 856 (2021) 158165.
[31] Y. Alshammari, F. Yang, L. Bolzoni, Mechanical properties and microstructure of Ti-Mn alloys produced via powder metallurgy for biomedical applications, J. Mech. Behav. Biomed. Mater. 91 (2019) 391–397.
[32] M. Alqattan, Y. Alshammari, F. Yang, L. Peters, L. Bolzoni, Biomedical Ti–Cu–Mn alloys with antibacterial capability, J. Mater. Res. Technol. 10 (2021) 1020–1028.
[33] ISO 10993-12 (2012) Biological Evaluation of Medical Devices-Part 12: Sample Preparation and Reference materials , Geneva , Switzerland, 2012.
[34] Y. Zhong, F. Yin, T. Sakaguchi, K. Nagai, K. Yang, Dislocation structure evolution and characterization in the compression deformed Mn–Cu alloy, Acta Mater. 55 (2007) 2747–2756.
[35] K.K. Alaneme, E.A. Okotete, Recrystallization mechanisms and microstructure development in emerging metallic materials: a review, Adv. Mater. Devices 4 (2019) 19–33.
[36] M. Kikuchi, Y. Takada, S. Kiyosue, M. Yoda, M. Woldu, Z. Cai, O. Okuno, T. Okabe, Mechanical properties and microstructures of cast Ti-Cu alloys, Dent. Mater. 19 (2003) 174–181.
[37] L. Pan, J. Gu, W. Zou, T. Qiu, H. Zhang, J. Yang, Brazing joining of Ti3AlC2 ceramic and 40Cr steel based on Ag-Cu-Ti filler metal, J. Mater. Process. Technol. 251 (2018) 181–187.
[38] X. Dai, J. Cao, Z. Chen, X. Song, J. Feng, Brazing SiC ceramic using novel B4C reinforced Ag–Cu–Ti composite filler, Ceram. Int. 42 (2016) 6319–6328.
[39] T. Zaharinie, Z. Huda, S. Ibrahim, F. Yusof, M. Hamdi, M. Rehan, T. Ariga, Analysis of the reaction layer formed during sapphire–sapphire brazing using a Ag–Cu–Ti filler metal for gas-pressure sensors, ACS Appl. Electron. Mater. 4 (2022) 2405–2412.
[40] L.W. Lin, J.M. Song, Y.S. Lai, Y.T. Chiu, N.C. Lee, J.Y. Uan, Alloying modification of Sn–Ag–Cu solders by manganese and titanium, Microelectron. Reliab. 49 (2009) 235–241.
[41] D.B. Lee, J.H. Woo, S.W. Park, Oxidation behavior of Ag-Cu-Ti brazing alloys, Mat. Sci. Eng. A. 268 (1999) 202–207.